

PHYSICS

Tracking the vector acceleration with a hybrid quantum accelerometer triad

Simon Templier^{1,2}, Pierrick Cheiney¹, Quentin d'Armagnac de Castanet^{1,2}, Baptiste Gouraud¹, Henri Porte¹, Fabien Napolitano¹, Philippe Bouyer^{1,3,4,5}, Baptiste Battelier^{2*}, Brynle Barrett^{1,2,6}

Robust and accurate acceleration tracking remains a challenge in many fields. For geophysics and economic geology, precise gravity mapping requires onboard sensors combined with accurate positioning and navigation systems. Cold atom-based quantum inertial sensors can potentially provide these high-precision instruments. However, current scalar instruments require precise alignment with vector quantities. Here, we present the first hybrid three-axis accelerometer exploiting the quantum advantage to measure the full acceleration vector by combining three orthogonal atom interferometer measurements with a classical navigation-grade accelerometer triad. Its ultralow bias permits tracking the acceleration vector over long time scales, yielding a 50-fold improvement in stability ($6 \times 10^{-8} g$) over our classical accelerometers. We record the acceleration vector at a high data rate (1 kHz), with absolute magnitude accuracy below $10 \mu g$, and pointing accuracy of $4 \mu rad$. This paves the way toward future strapdown applications with quantum sensors and highlights their potential as future inertial navigation units.

INTRODUCTION

Our ability to manipulate and control light and matter at the quantum level has opened a suite of quantum technologies that promises to provide revolutionary new sensors that feature both high accuracy and high sensitivity for a large variety of applications. Their ability to measure minute changes in inertial quantities such as accelerations and rotations with unprecedented performance in terms of accuracy, sensitivity, and long-term stability can lead to paradigmatic changes in our ability to navigate without external aid (1), monitor our planet (2), or test the predictions of physical theories (3–8). Today, matter-wave inertial sensors (9, 10) provide mature accelerometers that can measure gravity (11–14) and gravity gradients (15–19) to remotely detect massive objects or mass movements and can be used to anticipate major risks such as earthquakes, volcanic eruptions, and sea-level rise (20). These quantum accelerometers are also key elements for future autonomous positioning and navigation devices.

Acceleration is a vector and is therefore described by both its absolute magnitude (or norm) and pointing direction. Most matter-wave inertial sensors realized so far are scalar in nature; they measure the projection of the acceleration on a preferred orientation defined by the interrogation laser used for quantum manipulation. Laboratory-based gravimeters thus rely on a precise orientation with respect to the vertical direction (11, 13), while mobile operation requires mounting the sensor on a gyro-stabilized platform (14, 21). In both cases, real-time (RT) tracking of the acceleration is complex and thus limits the potential application of these sensors until a fully transportable three-dimensional (3D) vector-type sensor becomes available. Several groups have made encouraging

progress with multiaxis sensing, both theoretically (22, 23) and experimentally (24–28). However, none of these studies have gone beyond the proof-of-principle level. Our work takes a step toward a robust, motion-compatible instrument capable of measuring the full acceleration vector in real time.

Here, we report the first quantum accelerometer triad (QuAT), which measures accelerations along three mutually orthogonal directions. Our QuAT, shown in Fig. 1, consists of a hybrid 3D architecture combining cold atoms and classical accelerometers (29–31) to achieve high data rate (1 kHz), ultralow bias ($\sim 5 \mu g$) measurements of the three components of acceleration (a_x, a_y, a_z), with excellent long-term stability, reaching 60 ng on the vector norm ($|\mathbf{a}| = \sqrt{a_x^2 + a_y^2 + a_z^2}$) after 24 hours of integration in static conditions. After adapting broadly used accelerometer calibration methods to our hybrid triad (32), we estimate an accuracy of $7.7 \mu g$ on the vector norm, which is limited primarily by small misalignments between axes ($\sim 4 \mu rad$). Further improvements to the mechanical constraints of the system are anticipated to reduce systematics and improve accuracy by an order of magnitude. At this level, tilts of the tidal gravitational anomaly could be measured and used, for instance, to correct effects on large-area optical gyroscopes (33) or to further improve models of Earth's gravity (15, 34). This work also paves the way toward strapdown inertial navigation with quantum sensors and opens new possibilities for gravity mapping, mineral exploration, seismology, and monitoring climate change.

RESULTS

Each axis of the QuAT consists of a laser beam retroreflected by a mirror. These three orthogonal mirrors define the 3D reference frame with respect to which we measure the atom's motion (one axis at a time). Classical accelerometers are attached to the rear of each mirror to monitor their motion, as well as the component of gravitational acceleration. We then correct the frequency and phase of each laser to account for the motion of the atom relative to the corresponding mirror. This allows us to (i) suppress random phase noise due to mirror vibrations on each axis of the QuAT (29, 30),

Copyright © 2022
The Authors, some
rights reserved;
exclusive licensee
American Association
for the Advancement
of Science. No claim to
original U.S. Government
Works. Distributed
under a Creative
Commons Attribution
NonCommercial
License 4.0 (CC BY-NC).

¹IxBlue, 34 Rue de la Croix de Fer, 78105 Saint-Germain-en-Laye, France. ²Laboratoire Photonique, Numérique et Nanosciences (LP2N), Université Bordeaux-IOGS-CNRS: UMR 5298, 1 Rue François Mitterrand, 33400 Talence, France. ³Van der Waals-Zeeman Institute, Institute of Physics, University of Amsterdam, Science Park 904, 1098XH Amsterdam, Netherlands. ⁴QuSoft, Science Park 123, 1098XG Amsterdam, Netherlands. ⁵Eindhoven University of Technology, Eindhoven, Netherlands. ⁶Department of Physics, University of New Brunswick, 8 Bailey Dr., Fredericton, NB E3B 5A3, Canada. *Corresponding author. Email: baptiste.battelier@institutoptique.fr

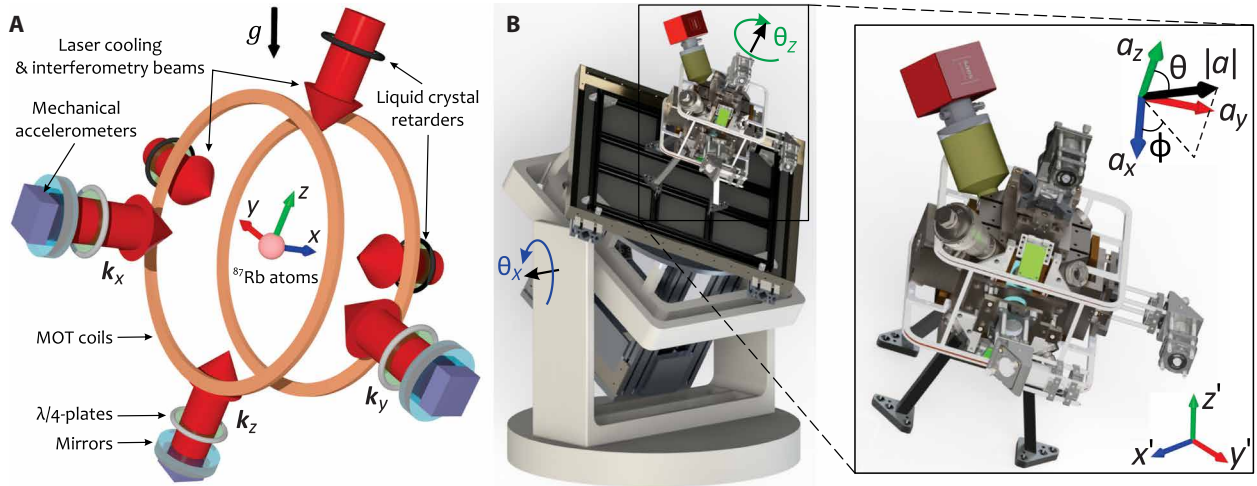


Fig. 1. QuAT. (A) Design concept and geometry of the QuAT. The acceleration components are measured along the wave vectors k_x , k_y , and k_z , which are perpendicular to the surface of their respective mirrors. MOT, magneto-optical trap. (B) 3D model of the sensor head mounted on a rotation stage that can be tilted about the z and x' axes by angles θ_z and θ_x , respectively. Applied in this order, these extrinsic rotations transform the coordinates from the laboratory frame ($x'y'z'$) to the body frame (xyz) of the QuAT. A cube-shaped μ -metal magnetic shield (not shown) surrounds the entire sensor head. The inset shows the Cartesian (a_x, a_y, a_z) and spherical polar (norm $|a|$, inclination θ , azimuth ϕ) coordinate representations of the acceleration vector in the body frame.

(ii) compensate for gravity-induced Doppler shifts in arbitrary orientations, and (iii) remove the bias of the classical accelerometers (31). To evaluate the accuracy of the QuAT, we developed a comprehensive model for systematic effects and we adapted a method for calibrating the triad over a large range of orientations (32). In the following, we detail the operation of the QuAT and present results characterizing its short- and long-term performance in different orientations (i.e., tilted with respect to gravity) while operating in a static environment.

Vectorial quantum accelerometer

Acceleration components are measured sequentially by switching between three Mach-Zehnder-type atom interferometers (10) using a $\pi/2$ - π - $\pi/2$ sequence of optical Raman pulses to split, reflect, and recombine matter waves. After an initial cooling and state selection phase, atoms are released into a geodetic free-fall trajectory. During this time, atoms experience a time-varying Doppler shift of $\omega_\mu^D = \mathbf{k}_\mu \cdot \mathbf{g}t$. As each atom interferometer forming the QuAT relies on velocity-sensitive Raman transitions, compensating for this shift is crucial for maintaining the lasers on the two-photon resonance. Atomic gravimeters typically achieve this by chirping the frequency difference between vertical Raman lasers at a quasi-constant rate of $\alpha = k$, thereby maintaining optimum fringe visibility. In an arbitrary orientation, the projection of gravity on each axis is different and, a priori, not precisely known, necessitating a closed-loop approach to compensate the Doppler shift. Moreover, strong mirror vibrations that blur the interference fringes and further shift the resonance condition (35) are a major concern. To address these issues, we implemented an RT system [inspired by the work in (36)] based on a field-programmable gate array (FPGA) that compensates both the frequency and phase of the Raman lasers during the interferometer using input from the classical accelerometers (see the Supplementary Materials). This system allows the QuAT to operate over a broad range of orientations and under noisy conditions. To leading order in T , the interferometer phase shift along each axis $\mu = x, y, z$ is

$$\Phi_\mu = (\mathbf{k}_\mu \cdot \mathbf{a} - \alpha_\mu) T^2 = (k_\mu a_\mu - \alpha_\mu) T^2 \quad (1)$$

where $\mathbf{k}_\mu = \frac{1}{c}(\omega_1 + \omega_2) \hat{\mu}$ is the effective wave vector of the counter-propagating Raman beams with optical frequencies ω_1 and ω_2 , respectively, α_μ is the effective chirp rate at which the Raman frequency is modified between pulses, T is the interrogation time between optical pulses, and \mathbf{a} is the acceleration vector of the atoms in the body frame (i.e., relative to the three orthogonal reference mirrors).

Figure 2 illustrates interference fringes obtained along each direction by varying α_μ . Data are shown for interrogation times $T = 5, 7, \text{ and } 10$ ms, where the fringe spacing in terms of acceleration is given by $2\pi/k_\mu T^2$. For each T , six fringes are measured by alternating between the axis μ and the momentum transfer $\pm \hbar \mathbf{k}_\mu$ in an interleaved sequence illustrated in Fig. 2C. Here, a negative (positive) momentum transfer indicates that the atoms are kicked toward (away from) the reference mirror. The central fringe for which $\mathbf{k}_\mu \cdot \mathbf{a} = \alpha_\mu$ provides a direct measurement of the acceleration component a_μ . The cycle time of our experiment is $T_{\text{cyc}} \approx 1.6$ s (limited by dead time generated by our control system); hence, a set of three measurements on orthogonal directions provides the full acceleration vector in under 5 s. We further improve our accuracy by combining measurements with opposite momentum kicks (see Materials and Methods), where one full measurement cycle is completed in $6T_{\text{cyc}} \approx 9.6$ s.

The data shown in Fig. 2 were acquired with the QuAT tilted at approximately $\theta_x = 54.7^\circ$ and $\theta_z = 45^\circ$ such that the gravitational acceleration points along the symmetry axis of the triad. In this orientation, the projection due to gravity along each axis is $a_\mu = g/\sqrt{3} \approx 5.66$ m/s², providing optimal sensitivity to the full acceleration vector \mathbf{a} . The transit time of the atoms across the Raman beams defines the maximum interrogation time achievable with the present architecture. When the cloud is released from rest at the center of the Raman beams, the maximum interrogation time is limited by the transit time of the atoms across the beams: $\frac{1}{2}a_\mu (\text{TOF} + 2T_{\text{max}})^2 = \sqrt{3}w_0$.

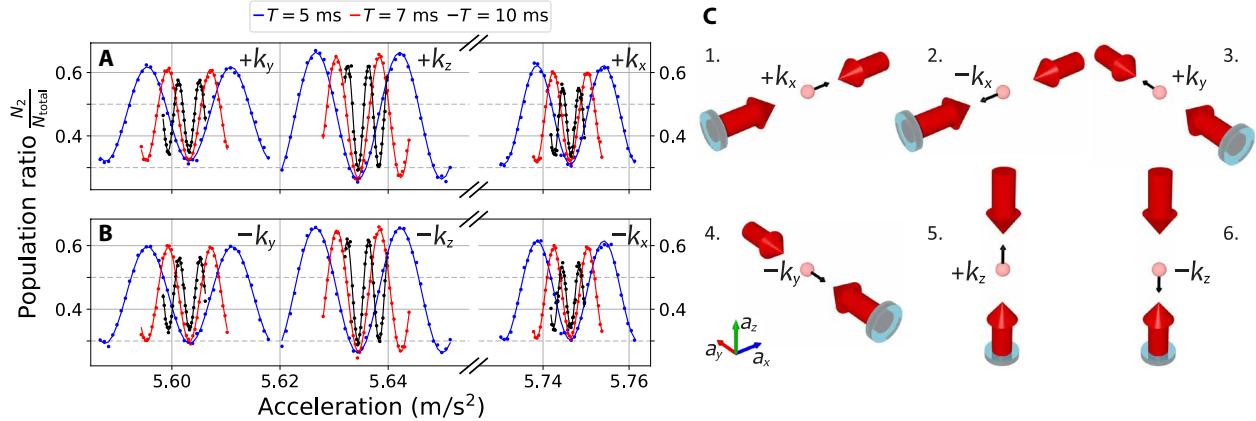


Fig. 2. Atom interferometry along three orthogonal axes. (A and B) Atomic interference fringes obtained along each axis μ (left, y ; middle, z ; and right, x) as a function of the laser-induced acceleration a_μ/k_μ . Plots (A) and (B) correspond to different momentum transfer directions ($\pm k_\mu$). Fringes are shown for interrogation times $T = 5$ ms (blue), 7 ms (red), 10 ms (black) at tilt angles of $\theta_x = 54.7^\circ$ and $\theta_z = 45^\circ$. The central fringe common to all T is visible in each set of fringes. (C) Sequence of measurement axes and corresponding momentum kicks used during one cycle of the QuAT. Pairs of opposite kicks provide one acceleration component with enhanced rejection of systematic effects.

For a time of flight TOF = 20 ms before the interferometer and a beam waist of $w_0 = 11$ mm, we obtain $T_{\text{max}} \approx 31$ ms. To maintain high signal-to-noise ratios on all axes, typically, we operate each axis of the QuAT at $T = 10$ ms, where we obtain fringe contrasts of $C_\mu = 0.20, 0.22,$ and 0.32 , and single-shot acceleration sensitivities of $\delta a_\mu = 11.9, 4.1, 5.1 \mu\text{g}$ for $\mu = x, y, z$, respectively. The corresponding sensitivity to the vector norm is $\delta|\mathbf{a}| = \frac{1}{g} \sqrt{\sum_\mu (a_\mu \delta a_\mu)^2} \approx 7.8 \mu\text{g}$.

To illustrate the effect of the RT system, Fig. 3 compares the fringe contrast on the y and z axes as a function of the tilt angle θ_x obtained with this system on and off. Here, the QuAT was oriented such that the yz plane was always vertical, and the tilt about the x axis (θ_x) was varied randomly over $\pm 90^\circ$. When the RT system is disabled (purple curve in Fig. 3B), the effective chirp rate is fixed such that the Doppler shift is compensated only for the vertical case, resulting in a maximum contrast on z when $\theta_x = 0$. As the z axis is tilted away from the vertical, there is a sharp drop in fringe contrast as the Raman pulses move further off resonance. When enabled, the RT system computes the Doppler shift from the acceleration component normal to the corresponding mirror. It then applies a sequence of phase-continuous frequency steps before each Raman pulse that approximates a chirp with an effective rate $\alpha_\mu = k_\mu \bar{a}_\mu$, where $\bar{a}_\mu = \frac{1}{2T} \int_0^{2T} a_\mu(t) dt$ is the average acceleration during the interferometer. In this case, $\alpha_y \approx k_y g \sin \theta_x$ and $\alpha_z \approx k_z g \cos \theta_x$. Figure 3 (A and B) shows that the RT system maintains a near-optimal fringe contrast over $>50^\circ$. Beyond this range, the contrast reduces because of other physical effects as we explain below. We emphasize that despite this drop in contrast, the sensitivity to accelerations remains relatively flat over a broad range of angles. Figure 3 (C and D) shows the acceleration sensitivity per shot: $\delta a_\mu = C_\mu / (2\sigma_D k_\mu T^2)$, where the fringe contrast C_μ and detection noise σ_D are obtained from fits to interference fringes. At $T = 10$ ms, we obtain $\delta a_\mu \lesssim 6 \mu\text{g}$ on each axis even at tilts of 60° .

The overall performance of the QuAT is optimal for measuring quasi-static acceleration vectors when it is tilted such that \mathbf{a} points along its symmetry axis. However, because of limitations of the present architecture, in other orientations, the sensitivity of one axis will improve at the expense of the others. This is exacerbated when one axis is nearly parallel with \mathbf{g} . The performance of the QuAT in

different orientations is important when considering the case of strapdown navigation (37), where dynamic movements cause both the magnitude and direction of the acceleration vector to change. In an arbitrary orientation, the acceleration sensitivity on any given axis is determined by the longitudinal and transverse motion of the atoms within the Raman beams. The present architecture relies on the Doppler shift of the atoms (generated by longitudinal motion in the beams) to isolate Raman transitions between $|F = 1, p_\mu\rangle$ and $|F = 2, p_\mu \pm \hbar k_\mu\rangle$. At near-horizontal orientations, the projection of gravity along the beam approaches zero, reducing the Doppler shift such that $|2, p_\mu + \hbar k_\mu\rangle$ becomes degenerate with several other states (e.g., $|2, p_\mu - \hbar k_\mu\rangle, |2, p_\mu\rangle, |2, p_\mu + 3\hbar k_\mu\rangle$). In this regime, double-diffraction processes (38, 39) and residual velocity-insensitive transitions cause a severe loss in transition probability between our target states. Furthermore, because of the Gaussian intensity profile of the Raman beams, motion in the plane transverse to the Raman wave vector causes a time-varying Rabi frequency during the interferometer. As T increases, the cloud moves toward the edge of the beams where the Rabi frequency approaches zero. These are the two primary effects that produce the contrast variation shown in Fig. 3.

We model the contrast as a function of θ_x with the RT system on and off, as shown by the solid curves in Fig. 3. Our model (see Materials and Methods), which contains only one free parameter, an arbitrary amplitude factor, shows remarkable agreement with the data. When the RT system is disabled, the contrast loss is dominated by the uncompensated Doppler shift $|k_\mu g (\cos \theta_x - 1)t|$ that increases markedly away from vertical ($\theta_x = 0$). When the RT system is enabled, the loss is determined by parasitic-diffraction processes, the Gaussian-shaped beam profile, and its finite size. On the z axis, we observe a strong asymmetry in the contrast about θ_x . This is explained by the fact that the initial cloud position is shifted by approximately -0.8 mm along the y axis relative to origin where the beams intersect. This results in a longer transit time across the beam for positive tilts ($\theta_x > 0$) compared to negative ones.

Tracking the acceleration vector

To illustrate the long-term performance of our instrument, we tracked the gravitational acceleration vector in the body frame (see Fig. 1)

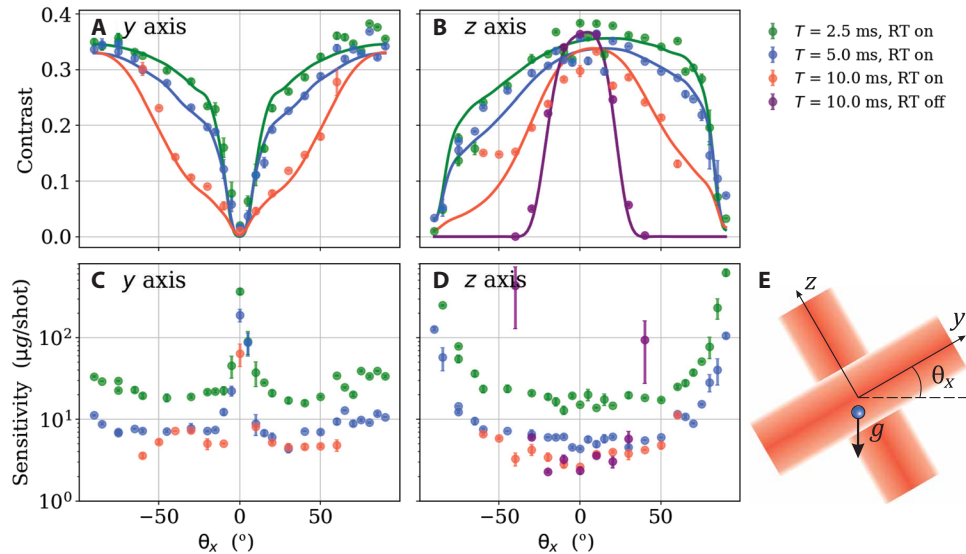


Fig. 3. Fringe contrast and acceleration sensitivity as a function of tilt angle. Interference fringe contrast (A and B) and acceleration sensitivity (C and D) along the y and z axes as a function of a random tilt angle θ_x . (E) Geometry of the Raman beams relative to the free-falling atoms. Data were recorded for various interrogation times with the RT system on (green points, $T = 2.5$ ms; blue points, $T = 5$ ms; and red points, $T = 10$ ms) and off (purple points, $T = 10$ ms). Error bars correspond to 1σ uncertainties obtained from sinusoidal fringe fits. Solid lines in (A) and (B) represent our model of the fringe contrast (see Materials and Methods for more details).

over 60 hours. During this experiment, the QuAT remained in a quasi-fixed orientation ($\theta_x = 45^\circ$, $\theta_z = 30^\circ$), and we operated it in closed loop with the classical accelerometers, creating a hybrid triad (see the discussion of Fig. 7 in Materials and Methods). Each axis of the QuAT is locked to its central fringe using a $\pm\pi/2$ phase modulation scheme (29, 40) similar to those used in atomic clocks. In this mode, each quantum accelerometer provides a high-accuracy measurement of the corresponding classical accelerometer bias (31). Data from the three classical accelerometers are simultaneously processed at a rate of 1 kHz, while their biases are sequentially subtracted from each axis at the cycling rate of the experiment (~ 0.6 Hz). In this manner, the hybrid triad retains the best features of both classical and quantum technologies.

Figure 4 shows an analysis of the hybrid triad output. We represent the acceleration vector in the body frame using both Cartesian (a_x , a_y , a_z) and spherical polar coordinates ($|\mathbf{a}|$, θ , ϕ). While both representations are equivalent, the latter best illustrates the physics that our instrument is capable of measuring. In Cartesian coordinates, all three vector components exhibit variations at the level of $\sim 5 \times 10^{-4}$ m/s². These changes could be produced by several different sources (e.g., uncompensated bias drifts in the classical accelerometers, changes in relative alignment between quantum accelerometer axes, or drifts of the triad's orientation with respect to \mathbf{g}). In spherical coordinates, it is clear that the vector norm $|\mathbf{a}|$ remains flat over 60 hours within our single-shot measurement noise ($\delta|\mathbf{a}| \sim 7.6 \times 10^{-5}$ m/s²). As any bias drifts or relative axis misalignments will affect $|\mathbf{a}|$, we can deduce that these two effects are below the noise level $\delta|\mathbf{a}|$. This places an upper limit on residual shot-to-shot bias variations of $\delta|\mathbf{a}|/\sqrt{3} \approx 4.4 \times 10^{-5}$ m/s² on each axis, as well as shot-to-shot misalignment variations of $\delta|\mathbf{a}|/\sqrt{3}g \approx 4.5$ μrad . However, the inclination and azimuth angles vary by approximately 70 and 20 μrad , respectively, over 60 hours. This indicates that the triad's orientation is slowly rotating relative to the gravity vector,

which produces correlated changes in the Cartesian acceleration components. This demonstrates sensitivity to rotations of the acceleration vector at the level of 10^{-10} rad/s.

Figure 4 also shows the Allan deviation of the acceleration vector norm produced by the hybrid and classical accelerometer triads. For time scales of $\tau \leq 1$ s, acceleration measurements from both triads are identical and dominated by correlated noise produced by ambient vibrations and the quantization of the analog signals, both of which integrate as $1/\tau$. After 1 s, the bias stability of each classical accelerometer begins to limit the performance of the classical triad, which reaches a minimum resolution of 7×10^{-7} g at 10 s. The norm of the classical triad shows evidence of continuous drift beyond 10 s. In contrast, the hybrid triad begins to stabilize this bias drift with a period $6 \times T_{\text{cyc}}$, where $T_{\text{cyc}} \approx 1.6$ s is the one-axis measurement cycle time. This results in a small improvement in the performance of the norm at short term, followed by a turning point near the cycle time of the full triad (9.6 s). The Allan deviation then increases until approximately 100 s as a result of the integrator time constant of our feedback loop. For time scales larger than this time constant, the Allan deviation integrates as $1/\sqrt{\tau}$, indicating white Gaussian noise. A fit to this section of the Allan deviation yields a sensitivity of $22 \mu\text{g}/\sqrt{\text{Hz}}$, which is limited primarily by the low cycling rate of our instrument. The vector norm of the hybrid triad reaches a stability of $\sigma_a = 6 \times 10^{-8}$ g after 24 hours of integration. In comparison, the classical triad drifts by $\sigma_a \approx 3 \times 10^{-6}$ g on the same time scale, indicating a 50-fold improvement in vector tracking capability. On time scales of a few hours, the horizontal position error of inertial navigation units is primarily limited by the bias stability of its accelerometers (37). These result in Schuler oscillations in the position with amplitude $\sigma_a R_E/g$ and a characteristic period $2\pi\sqrt{R_E/g} = 84$ min, where R_E is Earth's mean radius. Hence, a factor of 50 improvement in the bias stability is expected to decrease the short-term position error by the same amount.

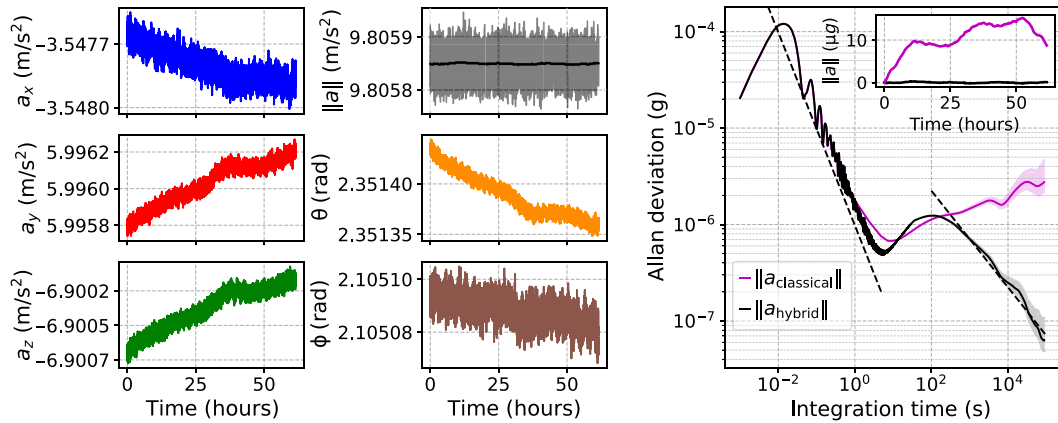


Fig. 4. Stability analysis of the hybrid accelerometer triad over 60 hours. Here, the interrogation time is $T = 10$ ms, and the sensor head is tilted at $\theta_x = 45^\circ$ and $\theta_z = 30^\circ$. **(Left)** Time series measurements of the hybrid acceleration on each axis in the body frame (a_x, a_y, a_z). These data are displayed at the cycling rate of the experiment. **(Middle)** Same data displayed in spherical polar coordinates with norm $|a| = \sqrt{a_x^2 + a_y^2 + a_z^2}$, inclination $\theta = \cos^{-1}(a_z/|a|)$, and azimuth $\phi = \text{atan2}(a_y, a_x)$. The solid black curve shows a 10-hour moving average of $|a|$. **(Right)** Allan deviation of acceleration vector norms as a function of integration time τ for the hybrid (black) and classical (purple) accelerometer triads. Dashed lines represent signals that integrate as $1/\tau$ and $1/\sqrt{\tau}$, respectively. Inset: Corresponding time series produced by the hybrid and classical accelerometer triads.

Systematic effects

In the previous section, we assessed the long-term stability of the hybrid accelerometer triad. We will now address the bias of the quantum accelerometers by evaluating the systematic effects of each atom interferometer. We also describe our calibration procedure to determine the overall accuracy of the instrument.

One major advantage of cold atom-based accelerometers over mechanical ones is their inherent accuracy. Systematic effects in atom interferometers have been studied extensively by several groups (3–8, 41, 42) and are well understood. However, most of the studies to date have considered atoms moving longitudinally along a vertical beam (e.g., as in a gravimeter or gradiometer). For the QuAT, the situation is more complex, as we must account for effects due to the atom's motion across three orthogonal beams in an arbitrary orientation. We developed a comprehensive model that allows us to vary key system parameters, such as the pulse timing, triad orientation, Raman beam intensities, and the magnetic bias fields. We used this model to characterize the systematic effects for each axis and aid the calibration procedure, which enabled us to evaluate the accuracy of the QuAT.

Table 1 provides a budget of systematic errors when the triad is tilted at 54.7° along its axis of symmetry, where all acceleration components have the same projection due to gravity. The largest systematic effect along any given axis is induced by our frequency-step protocol for the RT compensation of the Doppler effect. We apply a series of phase-continuous frequency steps to the Raman frequency that mimics a true frequency chirp between pulses but maintains a constant frequency during the pulses. This creates a slight imbalance between the kinematic phase due to atomic motion and the phase imprinted by the Raman laser, resulting in a phase shift proportional to the difference between the Rabi frequencies at the beamsplitter pulses

$$\phi_\mu^{\text{sys}} \approx -k_\mu a_\mu T(\pi/2 - 1)(\Omega_{\mu,3} - \Omega_{\mu,1})(2\tau_\mu/\pi)^2 \quad (2)$$

Here, $\Omega_{\mu,j}$ is the effective Rabi frequency along axis μ during Raman pulse j . In previous work (40), we evaluated this systematic

and its coupling to parasitic laser lines on the z axis. When oriented vertically, the shift due to the frequency-step protocol is $<1 \mu\text{g}$ at $T = 10$ ms. However, this effect is exacerbated in tilted configurations because the atoms experience a larger variation in the Rabi frequency as they transit the Raman beams. This also increases other systematic effects, such as the wavefront curvature (43), two-photon light shift (44), and the Coriolis effect. The latter cancels in the vector norm because the first-order shift due to Coriolis acceleration is proportional to $\sum a_\mu a_\mu^{\text{Coriolis}}$, which cancels if the initial launch velocity of the atom cloud is null. The uncertainty in this shift listed in Table 1 is due to the initial velocity uncertainties. Both the frequency-step shift and the two-photon light shift are proportional to the intensity of the Raman beams; hence, they can be suppressed in future iterations by subtracting measurements taken at two different intensities (45). This would reduce both effects by more than a factor of 10 at the expense of increased measurement time. Replacing the frequency-step protocol with a phase-continuous chirp would eliminate this systematic entirely. When coupled with minor improvements to the wavefront curvature, these enhancements would enable us to reduce the systematic uncertainty on each axis below 100 ng.

Figure 5 illustrates the complex dependence of the systematics on the orientation of the QuAT. As discussed above, the topology is governed primarily by three effects: our frequency-step protocol, the curvature of Raman wavefronts, and the two-photon light shift. All of these effects increase markedly when the beams are near horizontal. The frequency-step and wavefront systematics are dominated by the atoms sampling different regions of the Raman beam profile, while the two-photon light shift is strongly affected by the separation between neighboring Raman transitions. This effect produces regions in Fig. 5 with sharp changes in contrast, where velocity-insensitive or magnetically sensitive transitions are near resonant with the primary $|1, p_\mu\rangle \rightarrow |2, p_\mu \pm \hbar k_\mu\rangle$ transition. To evaluate the effect on the acceleration vector norm, we sum the systematic shifts on each axis weighted by the corresponding projection on norm. The results shown in Fig. 5D indicate that the systematic shift on the norm is largest in regions where the projections from each axis

Table 1. Systematic error budget. Systematic shifts for each axis of the QuAT when tilted along its symmetry axis ($\theta_x = 54.7^\circ$, $\theta_z = 45^\circ$). Here, we assume the axes of the QuAT are mutually orthogonal (i.e., no misalignments). Systematic shifts a_{μ}^{sys} are evaluated assuming that path-independent contributions are suppressed by 90% using k -reversal, with 1σ uncertainties given in parentheses. The systematic shift of the vector norm is $|a^{\text{sys}}| = \sum_{\mu} a_{\mu}^{\text{sys}} / |a|$ (to first order), where $a_x = -a_y = a_z \approx -5.66 \text{ m/s}^2$ in this orientation. Other parameters: TOF (time of flight) = 20 ms, $2\tau_{\mu} = (12, 11, 10) \mu\text{s}$, and $T = 10 \text{ ms}$; Rabi frequencies for velocity-sensitive transitions $\Omega_{x,1} = 0.299(75) \text{ rad}/\mu\text{s}$, $\Omega_{x,3} = 0.138(20) \text{ rad}/\mu\text{s}$, $\Omega_{y,1} = 0.273(55) \text{ rad}/\mu\text{s}$, $\Omega_{y,3} = 0.165(51) \text{ rad}/\mu\text{s}$, $\Omega_{z,1} = 0.316(75) \text{ rad}/\mu\text{s}$, and $\Omega_{z,3} = 0.200(78) \text{ rad}/\mu\text{s}$; Rabi frequencies for velocity-insensitive transitions $\Omega_{\mu,j}^{\text{co}} = 0.68(10) \Omega_{\mu,j}$; B -field strengths $B_x = 139.41(38) \text{ mG}$, $B_y = 137.70(27) \text{ mG}$, and $B_z = 147.71(73) \text{ mG}$; B -field gradients $\partial_x B_x = -0.045(19) \text{ G/m}$, $\partial_y B_y = 0.211(11) \text{ G/m}$, and $\partial_z B_z = -0.204(11) \text{ G/m}$; cloud temperature $\mathbb{T} = 3.5(1.0) \mu\text{K}$; initial cloud position and velocity uncertainties $\delta\mu = 0.2 \text{ mm}$ and $\delta v_{\mu} = 3 \text{ mm/s}$; and curvature of Raman wavefronts $R_x = 5.01(1.7) \text{ km}$, $R_y = 4.2(1.4) \text{ km}$, and $R_z = 4.2(1.4) \text{ km}$.

Systematic effect	a_x^{sys}	a_y^{sys}	a_z^{sys}	$ a^{\text{sys}} $	$\delta a^{\text{sys}} $	Unit
Frequency step	-57.9(3.8)	26.7(4.7)	-26.7(5.2)	64.3	4.6	μg
Wavefront curvature	1.69(73)	2.14(92)	2.02(87)	-0.91	0.84	μg
Two-photon light shift	-5.53(32)	6.15(43)	-4.58(19)	9.39	0.33	μg
Parasitic lines	0.02(30)	0.00(30)	-0.02(18)	0.00	0.26	μg
Coriolis effect	0.644(60)	-0.077(14)	-0.721(59)	0.000	0.049	μg
One-photon light shift	0.000(19)	0.000(12)	0.000(16)	0.000	0.016	μg
Quadratic Zeeman	-0.002(5)	0.008(3)	-0.008(3)	0.010	0.004	μg
RF nonlinearity	-0.011	0.011	-0.011	0.020	<0.001	μg
Total	-61.2(3.9)	34.9(4.8)	-30.1(5.4)	72.8	4.7	μg

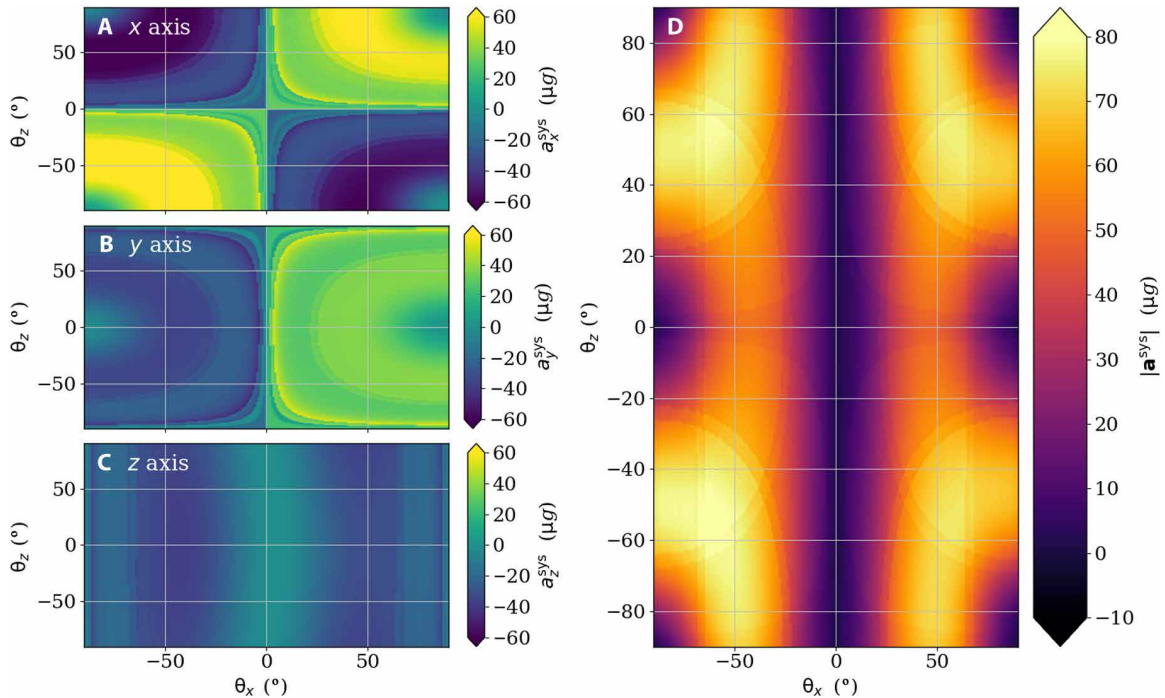


Fig. 5. Model of systematic shifts as a function of tilt angles θ_x and θ_z . The total shift a_{μ}^{sys} is shown for each axis of the QuAT (A to C), as well as the vector norm $|a^{\text{sys}}|$ (D). Experimental parameters are the same as for Table 1. All graphs show the mean of systematic shifts with opposite momentum transfer: $\frac{1}{2}[a_{\mu}^{\text{sys}}(+k_{\mu}) + a_{\mu}^{\text{sys}}(-k_{\mu})]$.

are similar in magnitude (e.g., near $\theta_x = \pm 54.7^\circ$, $\theta_z = \pm 45^\circ$), which is consistent with our expectations.

Calibration of the QuAT

Misalignments between axes and variations in the accelerometer scale factors directly affect both the magnitude and direction of the acceleration vector. The triad axes are defined by the effective wave

vectors \mathbf{k}_{μ} , which are normal to the surface of the corresponding retroreflection mirror. As these mirrors are oriented at approximately 90° relative to each other, the error in the acceleration vector scales to first order with misalignment angle. These misalignments are challenging to measure and stabilize at levels below $10 \mu\text{rad}$ because of mechanical strain and thermal expansion (15). In addition to misalignments, the accuracy of the QuAT is affected by the scale

factor of each quantum accelerometer ($S_\mu \approx k_\mu T^2$). These quantities depend on the absolute frequency of our Raman lasers, the angle between the incident and retroreflected Raman beams, the timing between laser pulses, and the beam intensity sampled by the atoms. To account for imperfections in the alignment and scale factors of the QuAT, we model its output in an arbitrary static orientation as follows

$$\begin{bmatrix} \tilde{a}_x \\ \tilde{a}_y \\ \tilde{a}_z \end{bmatrix} = \begin{bmatrix} \kappa_x & 0 & 0 \\ 0 & \kappa_y & 0 \\ 0 & 0 & \kappa_z \end{bmatrix} \begin{bmatrix} 1 & 0 & 0 \\ \lambda_{yx} & 1 & 0 \\ \lambda_{zx} & \lambda_{zy} & 1 \end{bmatrix} \begin{bmatrix} a_x \\ a_y \\ a_z \end{bmatrix} + \begin{bmatrix} a_x^{\text{sys}} \\ a_y^{\text{sys}} \\ a_z^{\text{sys}} \end{bmatrix} \quad (3)$$

where \tilde{a}_μ is a measured acceleration component, κ_μ is a relative scale factor, $\lambda_{\mu\nu}$ is the misalignment factor between axes μ and ν , and a_μ^{sys} is a systematic bias. Here, a_μ is the gravitational acceleration projected onto a mutually orthogonal Cartesian frame; hence, they obey $a_x^2 + a_y^2 + a_z^2 = g^2$, where $g = 9.805642 \text{ m/s}^2$ is the local gravitational acceleration. To estimate these parameters, we measured the gravity vector at several different orientations, as shown in Fig. 6. We then subtract orientation-dependent systematic shifts and fit our triad model (Eq. 3) to the resulting data using an iterative minimization algorithm (32). Table 2 summarizes the parameters that best fit the data, indicating misalignment angles up to $\lambda_{\mu\nu} \approx 200 \mu\text{rad}$ between axes and relative scale factors κ_μ within 50 parts per million of unity. These differ from unity primarily because of the finite pulse lengths τ_μ and the nonideal Rabi frequencies $\Omega_{\mu,j}$, which affect the atom interferometer scale factors according to (40, 46)

$$S_\mu = k_\mu(T + 2\tau_\mu) \left[T + \frac{1}{\Omega_{\mu,1}} \tan\left(\frac{\Omega_{\mu,1}\tau_\mu}{2}\right) + \frac{1}{\Omega_{\mu,3}} \tan\left(\frac{\Omega_{\mu,3}\tau_\mu}{2}\right) \right] \quad (4)$$

To convert our atom interferometer phase measurements to accelerations, we used a scale factor with ideal Rabi frequencies: $S_\mu^{\text{ideal}} = k_\mu(T + 2\tau_\mu)(T + 4\tau_\mu/\pi)$. For our experimental parameters, we find that the ratio between these scale factors varies between

$S_\mu/S_\mu^{\text{ideal}} \approx 0.999940$ to 0.999980 , which is consistent with the results shown in Table 2. The misalignment between the classical accelerometers and the quantum ones is absorbed into their respective scale factors. Effectively, the hybrid system forces these two triads to be aligned at the expense of slightly smaller classical accelerometer scale factors.

Figure 6 illustrates the effect of the triad calibration. Vector accelerations were recorded over tilt angles ranging from $\theta_x = -55^\circ$ to $+55^\circ$ and $\theta_z = -30^\circ$ to $+45^\circ$ (see Fig. 1 for reference). This large range of orientations causes the acceleration components to vary over roughly $\pm 5 \text{ m/s}^2$. Each orientation of the QuAT was set by carrying out a sequence of two extrinsic rotations: one about the vertical z axis with an angle θ_z , followed by a rotation about the horizontal x axis by θ_x . This sequence is described by the following transformation of the gravity vector

$$\begin{bmatrix} a_x \\ a_y \\ a_z \end{bmatrix} = \begin{bmatrix} \cos \theta_z & -\sin \theta_z \cos \theta_x & +\sin \theta_z \sin \theta_x \\ \sin \theta_z & +\cos \theta_z \cos \theta_x & -\cos \theta_z \sin \theta_x \\ 0 & \sin \theta_x & \cos \theta_x \end{bmatrix} \begin{bmatrix} 0 \\ 0 \\ -g \end{bmatrix} \quad (5)$$

The measured accelerations reflect this dependence on θ_x and θ_z , as shown in Fig. 6 (A to C). Small imperfections in the triad lead to substantial errors in the vector norm. Figure 6D shows that, in some orientations, the uncalibrated QuAT produces errors as large as $140 \mu\text{g}$. However, these errors are effectively corrected using the calibration

Table 2. QuAT model parameters resulting from the calibration procedure. The 1σ uncertainties are provided in parentheses. The scale factors are determined to about 3 parts per million. The uncertainty on the misalignment angles is approximately $4 \mu\text{rad}$, providing a direct metric of the vector pointing accuracy.

Scale factors	Misalignments
$\kappa_x = 0.9999563(41)$	$\lambda_{yx} = +1.926(42) \times 10^{-4} \text{ rad}$
$\kappa_y = 0.9999702(25)$	$\lambda_{zx} = +1.967(43) \times 10^{-4} \text{ rad}$
$\kappa_z = 0.9999619(18)$	$\lambda_{zy} = -1.359(25) \times 10^{-4} \text{ rad}$

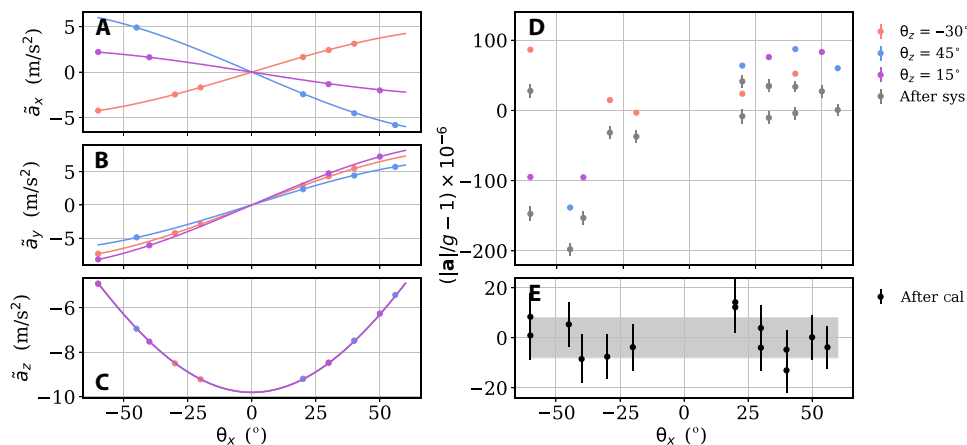


Fig. 6. Data used to calibrate the QuAT. The acceleration vector is sampled at 14 independent orientations (labeled by tilt angles θ_x and θ_z) using an integration time of $T = 10 \text{ ms}$. (A to C) Measured acceleration components \tilde{a}_x , \tilde{a}_y , and \tilde{a}_z for each orientation. Solid lines correspond to expected variations with θ_x . (D) Error in the vector norm before (colored) and after (gray) the subtraction of systematics. Error bars for the raw data are smaller than the points. (E) Zoom of the vector norm error after the calibration procedure. The gray band indicates the remaining RMS spread of $\pm 7.7 \mu\text{g}$.

procedure. We test the calibration by inverting Eq. 3 with the parameters in Table 2 to determine the true acceleration vectors. Before calibration, the root mean squared (RMS) error in the vector norm is 74 μg . After the calibration procedure, the RMS error decreases by almost an order of magnitude to 7.7 μg . We anticipate that further improvements can be gained by compensating the measurements for the variation of interferometer scale factors with orientation.

DISCUSSION

We have achieved full 3D tracking of the acceleration vector with a compact hybrid QuAT and demonstrated a 50-fold improvement in the long-term bias stability over navigation-grade accelerometers. Our instrument combines sequential interrogation of three single-beam atom interferometers coupled with a classical accelerometer triad. Fusion of all data from the QuAT provides the quantum advantage in short-term accuracy and low long-term bias drift together with the high data rate required to track the acceleration. Our RT compensation constitutes a significant advance in our capability to carry out measurements in arbitrary static orientations. Work is currently under way to tackle the issue of fringe contrast loss due to dynamic accelerations and rotations.

Accurate positioning and navigation often requires the fusion of data from global navigation satellite systems and autonomous inertial navigation systems (INSs). The latter heavily relies on triads of accelerometers and gyroscopes, where the attitude and position of a moving body are determined by integrating the equations of motion (37). The accuracy of an INS is limited by the bias stability of the inertial sensors (47, 48), as well as the knowledge of the local gravitational field. Taking advantage of the quantum nature of our sensor, its high sensitivity and low bias stability can resolve all these challenges (1, 31). It is sensitive to acceleration resulting from motion (AC) as well as from gravity (DC) and exhibits a long-term stability of 60 ng [60 microGalileos (μgal)]. The short-term (AC) sensitivity of the QuAT is mostly limited by the classical accelerometers to 100 μg at an interrogation time of $T = 10$ ms. Our model of systematic effects combined with our calibration procedure leads to a DC accuracy of 7.7 μg (7.7 mgal) on the vector norm and a pointing accuracy of ~ 4 μrad relative to each axis.

The results presented here demonstrate the full potential of matter-wave inertial sensors for future quantum-aided navigation, either by using the QuAT output to directly determine a vehicle's position or by providing strapdown operation for gravity mapping (14, 21) or gravity matching-aided navigation (49, 50). They can also be used to reduce the bias drift on the local acceleration readings and thus relieve the constraint on Schuler, Foucault, or other Earth-periodic oscillation errors (51). Our work is an essential step toward these onboard applications, yet further development is necessary before the instrument can be field qualified. This will include the compensation of rotation-induced effects to maintain the interferometer fringe contrast and avoid additional phase noise, improvements in mechanical rigidity and temperature sensitivity, and a characterization of the classical accelerometer frequency response and scale factor nonlinearity. Future work will involve the integration of classical gyroscopes for autonomous positioning and navigation applications, enabling us to reach the full potential of our QuAT.

The pointing accuracy of the QuAT, together with its long-term stability, provides a promising alternative for high-resolution tidal

tilt measurements (52). A correlated array of such accelerometer triads, or their combination with precision rotation measurements, can render angle measurements immune to external noise and improve our understanding of ground motion, representing a major stake for seismology. Long-term angle monitoring can provide knowledge of translational and rotational motion that could significantly improve seismic inverse models for Earth's structure (53), allow for full seismic signal reconstruction and modeling (54), or help characterize earthquake sources (55) and their points of origin (56).

MATERIALS AND METHODS

Here, we describe the apparatus, including the multiaxis sensor head, laser source, and the rotation platform. We also present our quantum-classical sensor hybridization scheme and outline our model for the interferometer fringe contrast.

Sensor head and laser system

To reduce the size and complexity of our apparatus, we adopted a three-beam architecture where retroreflected light along each axis can be used for trapping, cooling, manipulating, and detecting the atoms. This requires independent control of the optical power and polarization on each axis. Our design includes three optical collimators that expand the light to a $1/e^2$ diameter of ~ 22 mm and three retroreflection mirrors to which we attach mechanical accelerometers for hybridization purposes. We use navigation-grade pendulous rebalance accelerometers manufactured by Thales (J192AAM on the x and y axes, EMA 1000-B1 on the z axis), which feature a high-sensitivity and high-bandwidth response. They feature an intrinsic bias between 50 and 180 μg , a scale factor variation of 120 parts per million/ $^\circ\text{C}$, a flat response from DC to approximately 300 Hz, and a monotonically decreasing sensitivity up to ~ 1 kHz. For the hybridization process, we acquire raw data from these sensors at 5 kHz. The output of the hybrid sensor is digitally filtered before being streamed to disc at a data rate of 1 kHz. These accelerometers also feature a magnetic shield, which is crucial for reducing their sensitivity to the relatively strong, pulsed magnetic fields produced by nearby magneto-optical trap (MOT) coils.

All of the optics are fixed directly to a forged titanium vacuum chamber, forming the rigid triad shown in Fig. 1B. Magnetic bias and gradient coils required for atom trapping and interferometry are wound within circular grooves machined directly on the x and y axes of the chamber. Two pairs of square coils fixed outside the chamber provide both a bias field and a gradient field on the z axis. The entire vacuum system is mounted within a single-layer μ -metal shield to stabilize the B -field experienced by the atoms when the system is rotated. Excluding the magnetic shield, the volume of the sensor head is approximately 45 liters and weighs 40 kg. This includes the vacuum chamber, ion pump, fiber collimators, and detectors.

An all-fibered optical bench at 780 nm, mounted within the shield, includes polarizing cube-based fiber splitters (Thorlabs PBC780PM-APC), and a 1×4 micro-optic fiber switch (Leoni EOL 1x4) to alternate between cooling on all axes and interferometry on each axis. The light is produced by a unique dual-frequency laser source developed by iXblue (Modbox laser, 6U, 19-inch rack mounted) based on telecom components at 1560 nm and wavelength conversion to 780 nm in a periodically poled lithium niobate waveguide (NTT WH-0780-000-F-B-C). This laser source, which uses a unique

optical In-phase & Quadrature (IQ) modulator to derive all required frequencies, is described in detail elsewhere (40, 57). An oven-controlled liquid crystal retarder (LCR; Thorlabs LCC1111T-B) is placed at the output of each collimator, which allows us to switch between the polarizations required for cooling (circular) and coherent Raman transitions (linear) during the measurement sequence. We maintain the LCRs at a temperature of $\sim 53^\circ\text{C}$ to stabilize the switching time between polarization states ($\sim 500\ \mu\text{s}$ from circular to linear). A $\lambda/4$ -wave plate is also mounted in front of each retro-reflection mirror to flip the polarization on the return path (see Fig. 1A). This ensures that counterpropagating beams for cooling and trapping have opposite circular polarization, and the Raman beams have perpendicular linear polarization, allowing us to minimize parasitic velocity-insensitive transitions.

From the vapor-loaded 3D MOT, we obtain approximately 10^8 ^{87}Rb atoms in 250 ms. This sample is subsequently cooled to approximately $3\ \mu\text{K}$ in a gray molasses on the D2 transition at $780\ \text{nm}$ (58). We prepare these atoms in the magnetically insensitive $|F=1, m_F=0\rangle$ state by (i) initially pumping them to $|F=1\rangle$, (ii) applying a quantizing B -field of $140\ \text{mG}$ along a given axis ($\mu = x, y, z$), and (iii) removing atoms in the $|F=1, m_F=\pm 1\rangle$ states through a coherent optical transfer to $|F=2\rangle$, followed by a near-resonant push pulse (57). To measure different acceleration components, we switch between axes sequentially using the independent Raman beams and corresponding pairs of Helmholtz coils. At this point, the two Raman beams are detuned by $\Delta_R = -880\ \text{MHz}$ from the $|F'=2\rangle$ excited state in ^{87}Rb , and we apply a $\pi/2$ - π - $\pi/2$ sequence of Raman pulses separated by interrogation time T . This is followed by a fluorescence detection phase where a sequence of near-resonant pulses is applied along the z axis to measure the ratio of atoms in $|F=2\rangle$. Our detection system is composed of two photodiodes with large fields of view to measure the fluorescence from the atoms over a broad range of orientations. The effective detection volume of this system is a sphere with a diameter of approximately $26\ \text{mm}$. This enables us to observe fluorescence up to flight times of $\sim 52\ \text{ms}$. The detection signal is digitized and processed to determine the acceleration component on a given axis.

This sequence of operations occurs once per measurement cycle ($T_{\text{cyc}} \approx 1.6\ \text{s}$), which is limited by software dead time (59). A minimum of two measurement cycles are required to obtain one acceleration component (one on each side of the interference fringe at $\pm\pi/2$); hence, the full acceleration vector can be obtained in six measurement cycles ($\sim 9.6\ \text{s}$). However, in practice, we use 6 cycles with a momentum transfer direction $+\mathbf{k}_\mu$ interleaved with 6 cycles using $-\mathbf{k}_\mu$ to reject path-independent systematic biases on each axis. Hence, we construct the full acceleration vector once every 12 cycles ($\sim 19.2\ \text{s}$).

Rotation platform

The QuAT is installed on a manual three-axis rotation platform that can be rotated continuously by 360° about three independent axes. This platform was initially designed for small loads and had to be modified to accommodate the QuAT. To compensate for the mass of the sensor head ($40\ \text{kg}$) and the magnetic shield ($40\ \text{kg}$), we constructed an 80-kg ballast system below the primary platform. This keeps the center of mass near the center of rotation, minimizing the torque on the bearings. However, because of mechanical constraints of this system, the horizontal x axis was limited to rotation angles of $\theta_x \in [-90^\circ, +90^\circ]$ and the vertical z axis to angles $\theta_z \in [-180^\circ, +180^\circ]$ in steps of 15° . This freedom allows us to project different

amounts of gravity along each axis, which creates unique Doppler shifts due to the atom's free fall and breaks the degeneracy between $\pm\hbar\mathbf{k}_\mu$ momentum transfers. The general form of the Doppler shift is

$$\omega_\mu^D(t) = \pm k_\mu \int_0^t a_\mu(t') dt' \approx \pm k_\mu \bar{a}_\mu t \quad (6)$$

where the explicit time dependence of $a_\mu(t)$ accounts for the motion of the atoms relative to the surface of the mirror during the interferometer sequence and the \pm corresponds to opposite momentum transfers. The approximate form in Eq. 6 is valid when the variations in acceleration during the interferometer are negligible. Here, $\bar{a}_\mu = \frac{1}{2T} \int_0^{2T} a_\mu(t') dt'$ is the average acceleration during the interferometer. At any time t , the resonance condition is determined by the two-photon detuning δ_μ given by

$$\delta_\mu(t) = \Delta\omega_\mu^R(t) - \omega_{\text{HF}} - \omega_\mu^D(t) - \omega_{\text{rec}} \quad (7)$$

where $\Delta\omega_\mu^R(t)$ is the difference between optical Raman frequencies, $\omega_{\text{HF}} \approx 2\pi \times 6.834\ \text{GHz}$ is the ground-state hyperfine splitting, and $\omega_{\text{rec}} \approx 2\pi \times 15.1\ \text{kHz}$ is the recoil frequency for ^{87}Rb . For clarity, we have ignored smaller frequency shifts (e.g., due to the AC Stark effect) in Eq. 7. The resonance condition ($\delta_\mu = 0$) must be satisfied to optimize the transfer efficiency between the two target states ($|1, p\rangle$ and $|2, p \pm \hbar\mathbf{k}_\mu\rangle$). Hence, to maximize the fringe contrast of the atom interferometer at interrogation times $T > \Omega_\mu / |k_\mu \bar{a}_\mu|$, one must compensate the time-varying Dopplershift experienced by the free-falling atoms. This is typically achieved by applying a phase-continuous chirp to the Raman frequency: $\Delta\omega_\mu^R(t) \approx \omega_{\text{HF}} + \omega_{\text{rec}} + \alpha_\mu t$, where $\alpha_\mu = \pm k_\mu \bar{a}_\mu$. This maintains the resonance condition as the atoms accelerate toward or away from the mirror. In a fixed orientation, the chirp rate is constant for each axis and can be determined experimentally by locating the central fringe for which the total interferometer phase is zero (see Eq. 1). However, if the orientation of the triad is not precisely known, then determining α_μ with this method can be very time consuming. Furthermore, if the system is rotating or undergoing translational acceleration (i.e., if the triad is mobile), then α_μ needs to be updated on a shot-to-shot basis. In the most extreme case, when mirror accelerations exceed $a_\mu(t) > \Omega_\mu / k_\mu T$, the Doppler shift cannot be approximated as linear (30, 35) and must be compensated during the interferometer sequence. All of these scenarios can be addressed with an RT solution. We describe in detail our RT system in the Supplementary Materials.

Hybridization of the quantum and classical accelerometers

We hybridize the quantum and classical triads by establishing a feedback loop between the quantum phase measurements and the classical accelerometer signals. The hybridization can be understood as follows: The surfaces of the three retroreflection mirrors define the 3D reference frame for the atoms, and the relative motion of the triad compared to the free-falling atoms is recorded by the classical accelerometers. Because of ambient vibrations, the reference frame shakes and, by itself, produces phase noise on our interference fringes. To solve this issue, our RT system effectively stabilizes the Raman beams to the atoms' free-falling frame by correcting their relative frequency and phase. This allows us to suppress vibration noise on each axis of the QuAT, as well as to periodically measure

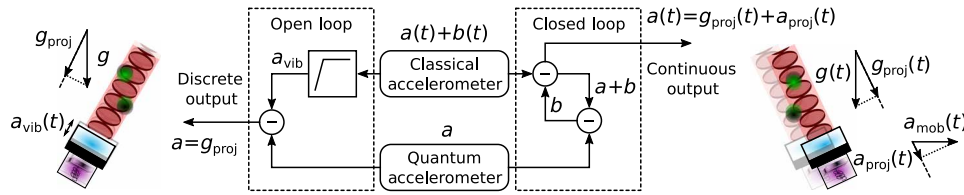


Fig. 7. Hybridization schemes between the quantum and classical accelerometers. The open-loop scheme on the left depicts how the filtered classical accelerometer is used to correct vibrations of the reference mirror a_{vib} for the quantum accelerometer. When static, the quantum accelerometer provides discrete measurements of the projection due to gravity g_{proj} . The closed-loop scheme on the right shows how the classical accelerometer is periodically bias-corrected by comparing its output to that of the quantum accelerometer. Here, the output of the hybrid accelerometer is continuous and functions in both static and dynamic cases, providing the sum of the projections due to gravity and motion-induced acceleration a_{proj} .

the bias of each classical accelerometer. These biases are then subtracted from the continuous output of the classical accelerometers once per measurement cycle and fed back to the QuAT one axis at a time, closing the feedback loop. In this way, we generate an ultrastable, high-bandwidth hybrid accelerometer triad.

Figure 7 illustrates the two hybridization schemes corresponding to the open-loop and closed-loop modes of the RT system. Open-loop mode provides direct measurements of the static accelerations (e.g., due to gravity) by suppressing the vibration noise in the quantum accelerometer (36). However, this mode is not optimized for operating under dynamic conditions where the QuAT is moving because the Doppler shift is not actively compensated. In closed-loop mode, the quantum accelerometer provides a measure of the classical accelerometer bias, which is then subtracted from its raw output. In this mode, the hybrid accelerometer triad can be operated in almost any orientation, as well as during dynamic motion.

To demonstrate the capability of the closed-loop hybridization scheme, Fig. 8 shows acceleration measurements as the tilt angle θ_x varies in discrete steps over 50° . Here, the acceleration varies as $a_y = g \sin \theta_x$ and $a_z = -g \cos \theta_x$ because $\theta_z = 0$. As a result of the finite bandwidth of the central-fringe lock, the vector norm shows sharp features whenever the tilt changes abruptly. After each 5° jump in θ_x , the vector norm settles back to its nominal value of 9.805 m/s^2 regardless of the triad's orientation. Figure 8B shows the classical accelerometer biases measured by the hybrid system. Small misalignments with the axes of the quantum triad produce coupling with the scale factors of the classical sensors, resulting in artificial bias variations with θ_x .

Model of the fringe contrast

The fringe pattern for each atom interferometer has the simple sinusoidal form

$$P_\mu = A_\mu - B_\mu(\Phi_\mu) \quad (8)$$

where P_μ is the probability of measuring the atom in $|F = 2\rangle$, A_μ is the fringe offset (typically $\approx 1/2$), and $B_\mu(\Phi_\mu)$ is an interference term given by $B_\mu = \frac{1}{2}C_\mu \cos \Phi_\mu$ with fringe contrast C_μ . We showed in Fig. 3 that C_μ varies strongly with the tilt of the triad because of the changing transfer efficiency of Raman transitions between the two target states. Here, we derive our model for the fringe contrast and show how it is affected by several experimental parameters. In what follows, we have dropped the subscript μ to simplify the notation.

Following the work of several other groups (60–62), for an ideal two-level atom, we can derive an analytical expression for the fringe

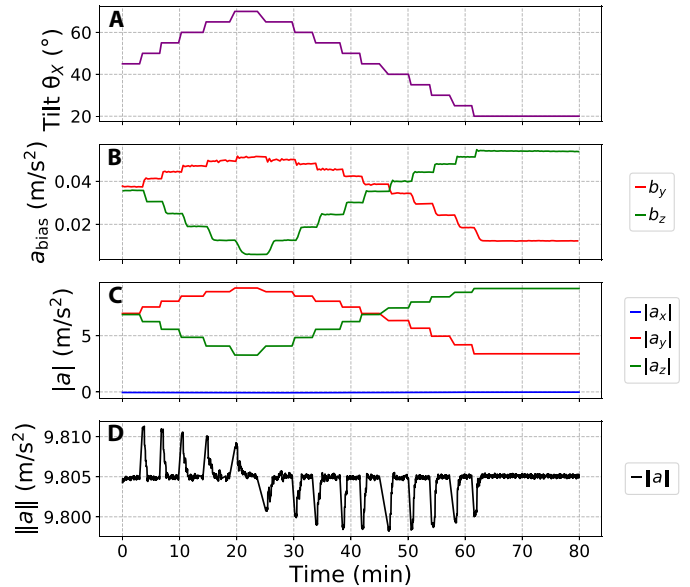


Fig. 8. Output of the hybrid accelerometer triad operating in closed-loop mode. The tilt angle θ_x is varied in 5° steps over 50° . Here, the interrogation time is $T = 5 \text{ ms}$ and $\theta_z = 0$. (A) Tilt of the triad as a function of time. (B) Classical accelerometer biases measured by quantum accelerometers. These vary with the tilt angle due to a small contribution from the scale factors of the classical accelerometers. (C) Magnitude of the acceleration components. (D) Acceleration vector norm output by the hybrid triad.

pattern. Under the rotating-wave approximation and ignoring spontaneous emission, the Hamiltonian describing a two-level atom interacting with a laser field is given by

$$\hat{H}(t) = \frac{\hbar}{2} \begin{bmatrix} \delta(t) & \bar{\Omega}(t) e^{-i\phi(t)} \\ \bar{\Omega}(t) e^{i\phi(t)} & -\delta(t) \end{bmatrix} \quad (9)$$

In our case, $\delta(t)$ represents the two-photon Raman detuning, $\bar{\Omega}(t) = \sqrt{\delta^2 + \Omega^2}$ is the generalized Rabi frequency with two-photon Rabi frequency $\Omega(t)$, and $\phi(t)$ is the phase of the laser field at time t . The time evolution of a wave function on the basis of bare-atom states $|\psi(t)\rangle = \alpha_0(t)|1, p\rangle + \beta_1(t)|2, p + \hbar k\rangle$ can be obtained from the following unitary transformation

$$\hat{U}(t, t') = \hat{\mathcal{T}} \exp \left[-\frac{i}{\hbar} \int_{t'}^t \hat{H}(u) du \right] \quad (10)$$

where \hat{T} is the time-ordering operator and α_0 and β_1 are complex state amplitudes that obey $|\alpha_0(t)|^2 + |\beta_1(t)|^2 = 1$. Henceforth, quantities labeled with the subscript j represent the value of that quantity during the j th Raman pulse with duration τ_j . For short optical pulses, we can approximate the optical phase, detuning, and Rabi frequency in Hamiltonian Eq. 9 to be time independent. The matrix exponential in Eq. 10 then has a closed-form expression

$$\hat{U}(t_j, t_j + \tau_j) \equiv \hat{U}_j = \exp \left[-\frac{i}{\hbar} \hat{H}(t_j) \tau_j \right] = \begin{bmatrix} c_j^* & -is_j^* \\ -is_j & c_j \end{bmatrix} \quad (11)$$

where the matrix elements contain

$$c_j = \cos \left(\frac{\Theta_j}{2} \right) + i \frac{\delta_j}{\tilde{\Omega}_j} \sin \left(\frac{\Theta_j}{2} \right), \quad s_j = \frac{\Omega_j e^{i\phi_j}}{\tilde{\Omega}_j} \sin \left(\frac{\Theta_j}{2} \right) \quad (12)$$

with pulse area $\Theta_j \equiv \tilde{\Omega}_j \tau_j$.

To obtain the fringe pattern Eq. 8 for a Mach-Zehnder atom interferometer, which consists of a $\pi/2$ - π - $\pi/2$ sequence of Raman pulses, we compute the probability for the transition $|1, p\rangle \rightarrow |2, p + \hbar k\rangle$ resulting from the corresponding product of unitary transformations

$$P = |\langle 2 | \hat{U}_3 \hat{U}_2 \hat{U}_1 | 1 \rangle|^2 \equiv A - B \quad (13A)$$

$$A = |s_1|^2 |s_2|^2 |s_3|^2 + |c_1|^2 |s_2|^2 |c_3|^2 + |s_1|^2 |c_2|^2 |c_3|^2 + |c_1|^2 |c_2|^2 |s_3|^2 \quad (13B)$$

$$B = c_1 s_1 (s_2^*)^2 c_3^* s_3 + \text{c.c.} \quad (13C)$$

When the pulse areas $\Theta_1 = \Theta_3 = \pi/2$ and $\Theta_2 = \pi$, the offset A reduces to

$$A = \frac{\Omega_1^2 \delta_2^2 \delta_3^2 + \tilde{\Omega}_1^2 \delta_2^2 \Omega_3^2 + \Omega_1^2 \Omega_2^2 \tilde{\Omega}_3^2 + \delta_1^2 \Omega_2^2 \tilde{\Omega}_3^2 + \delta_1^2 \Omega_2^2 \delta_3^2}{2 \tilde{\Omega}_1^2 \tilde{\Omega}_2^2 \tilde{\Omega}_3^2} \approx \frac{1}{2} \quad (14)$$

The approximation in Eq. 14 corresponds to the near-resonant case when $|\delta_j| \ll \Omega_j$. Similarly, the interference term can be written as

$$B = 2 |c_1| |s_1| |s_2|^2 |c_3| |s_3| \cos \Phi \equiv \frac{1}{2} C \cos \Phi \quad (15)$$

where $\Phi = \arg [c_1 s_1 (s_2^*)^2 c_3^* s_3] \approx \phi_1 - 2\phi_2 + \phi_3$ is the phase shift introduced by the laser field. Here, we have omitted phase contributions from the atom's external motion relative to the laser field, as well as small terms due to $\arg(c_1 c_3^*)$ that are linked to the asymmetry of the Mach-Zehnder interferometer (63). Combining Eqs. 12 and 15 and keeping only leading-order terms, the contrast is given by

$$C = 4 \frac{\Omega_1 \Omega_2^2 \Omega_3}{\tilde{\Omega}_1^2 \tilde{\Omega}_2^2 \tilde{\Omega}_3^2} \sin \frac{\Theta_1}{2} \sin^2 \frac{\Theta_2}{2} \sin \frac{\Theta_3}{2} \times \left(\delta_1 \delta_3 \sin \frac{\Theta_1}{2} \sin \frac{\Theta_3}{2} - \tilde{\Omega}_1 \tilde{\Omega}_3 \cos \frac{\Theta_1}{2} \cos \frac{\Theta_3}{2} \right) \quad (16)$$

This expression is equivalent to equation 3 in (63) with an explicit dependence on the two-photon detuning during each pulse. This allows us to model the behavior of the contrast for uncompensated Doppler shifts (i.e., when the RT system is disabled), as well as the effect of the velocity distribution by replacing $\delta_j = kv(t_j)$ and evaluating the velocity-averaged contrast

$$\bar{C} = \int N(v) C(v) dv \quad (17)$$

Here, $N(v) = \exp[-(v/\sigma_v)^2]/\sqrt{\pi} \sigma_v$ is the velocity probability density with $1/e$ velocity spread $\sigma_v = \sqrt{2k_B T/M}$.

Equation 16 is valid for a two-level atom and is generally accurate when the Doppler shift $\omega_D \gg \Omega$, ω_{rec} , where losses due to parasitic Raman transitions can be neglected. However, this condition is not satisfied when the Raman beam approaches horizontal, and the effects due to higher-order diffraction and velocity-insensitive transitions must be included. Using an approach similar to that in (39), we model these effects by numerically solving the full system of coupled differential equations given by

$$\dot{\alpha}_n = i\chi e^{+i[\delta+2\omega_D+2n\omega_{\text{rec}}]t} \beta_{n-1} + i\chi e^{+i[\delta-2n\omega_{\text{rec}}]t} \beta_{n+1} + i\chi_{\text{co}} e^{+i(\delta+\omega_D+\omega_{\text{rec}})t} \beta_n \quad (18A)$$

$$\dot{\beta}_n = i\chi_{\text{co}} e^{-i(\delta+\omega_D+\omega_{\text{rec}})t} \alpha_n \quad (18B)$$

$$\dot{\alpha}_{n+1} = i\chi_{\text{co}} e^{+i(\delta+\omega_D+\omega_{\text{rec}})t} \beta_{n+1} \quad (18C)$$

$$\dot{\beta}_{n+1} = i\chi e^{-i[\delta-2n\omega_{\text{rec}}]t} \alpha_n + i\chi e^{-i[\delta+2\omega_D+2(n+2)\omega_{\text{rec}}]t} \alpha_{n+2} + i\chi_{\text{co}} e^{-i(\delta+\omega_D+\omega_{\text{rec}})t} \alpha_{n+1} \quad (18D)$$

Here, $\alpha_n(t)$ and $\beta_n(t)$ are the probability amplitudes corresponding to the ground and excited states $|1, p + n\hbar k\rangle$ and $|2, p + n\hbar k\rangle$, respectively; $\chi \equiv \Omega/2$ is the half-Rabi frequency for velocity-sensitive Raman transitions, $\chi_{\text{co}} \equiv \Omega_{\text{co}}/2$ is the half-Rabi frequency for velocity-insensitive copropagating transitions, and δ is given by Eq. 7. We solve Eqs. 18A to 18D over the time interval of each pulse ($t_j \rightarrow t_j + \tau_j$) to obtain the state amplitudes $\alpha_{n=0,j}$ and $\beta_{n=1,j}$. Respectively, these amplitudes are generalizations of the c_j and s_j when including higher-order momentum transfer. Hence, following Eq. 15, we compute the fringe contrast using

$$C = 4 |\alpha_{0,1}| |\beta_{1,1}| |\beta_{1,2}|^2 |\alpha_{0,3}| |\beta_{1,3}| \quad (19)$$

SUPPLEMENTARY MATERIALS

Supplementary material for this article is available at <https://science.org/doi/10.1126/sciadv.add3854>

REFERENCES AND NOTES

1. C. Jekeli, Navigation error analysis of atom interferometer inertial sensor. *J. Inst. Nav.* **52**, 1–14 (2005).
2. T. Lévêque, C. Fallet, M. Manda, R. Biancale, J. M. Lemoine, S. Tardivel, S. Delavault, A. Piquereau, S. Bourgogne, F. Pereira dos Santos, B. Battelier, P. Bouyer, Gravity field mapping using laser-coupled quantum accelerometers in space. *J. Geodyn.* **95**, 1432–1394 (2021).
3. G. Rosi, F. Sorrentino, L. Cacciapuoti, M. Prevedelli, G. M. Tino, Precision measurement of the Newtonian gravitational constant using cold atoms. *Nature* **510**, 518–521 (2014).
4. R. Parker, C. Yu, Z. Weicheng, E. Brian, H. Müller, Measurement of the fine-structure constant as a test of the standard model. *Science* **360**, 191–195 (2018).
5. L. Morel, Z. Yao, P. Cladé, S. Guellati-Khélifa, Determination of the fine-structure constant with an accuracy of 81 parts per trillion. *Nature* **588**, 61–65 (2020).
6. P. Asenbaum, C. Overstreet, M. Kim, J. Curti, M. A. Kasevich, Atom-interferometric test of the equivalence principle at the 10^{-12} level. *Phys. Rev. Lett.* **125**, 191101 (2020).
7. L. Zhou, C. He, S.-T. Yan, X. Chen, D.-F. Gao, W.-T. Duan, Y.-H. Ji, R.-D. Xu, B. Tang, C. Zhou, S. Barthwal, Q. Wang, Z. Hou, Z.-Y. Xiong, Y.-Z. Zhang, M. Liu, W.-T. Ni, J. Wang, M.-S. Zhan, Joint mass-and-energy test of the equivalence principle at the 10^{-10} level using atoms with specified mass and internal energy. *Phys. Rev. A* **104**, 022822 (2021).
8. B. Barrett, G. Condon, L. Chichet, L. Antoni-Micollier, R. Arguel, M. Rabault, C. Pelluet, V. Jarlaud, A. Landragin, P. Bouyer, B. Battelier, Testing the universality of free fall using correlated ^{39}K - ^{87}Rb interferometers. *AVS Quantum Sci.* **4**, 014401 (2022).

9. C. J. Bordé, Atomic interferometry with internal state labelling. *Phys. Lett. A* **140**, 10–12 (1989).
10. M. A. Kasevich, S. Chu, Atom interferometry using stimulated Raman transitions. *Phys. Rev. Lett.* **67**, 181–184 (1991).
11. C. Freier, M. Hauth, V. Schkolnik, B. Leykauf, M. Schilling, H. Wziontek, H. G. Scherneck, J. Müller, A. Peters, Mobile quantum gravity sensor with unprecedented stability. *J. Phys. Conf. Ser.* **723**, 012050 (2016).
12. K. S. Hardman, P. J. Everitt, G. D. McDonald, P. Manju, P. B. Wigley, M. A. Sooriyabandara, C. C. N. Kuhn, J. E. Debs, J. D. Close, N. P. Robins, Simultaneous precision gravimetry and magnetic gradiometry with a Bose-Einstein condensate: A high precision, quantum sensor. *Phys. Rev. Lett.* **117**, 138501 (2016).
13. V. Ménoret, P. Vermeulen, N. L. Moigne, S. Bonvalot, P. Bouyer, A. Landragin, B. Desruelle, Gravity measurements below 10^{-9} g with a transportable absolute quantum gravimeter. *Sci. Rep.* **8**, 12300 (2018).
14. Y. Bidel, N. Zahzam, A. Bresson, C. Blanchard, M. Cadoret, A. V. Olesen, R. Forsberg, Absolute airborne gravimetry with a cold atom sensor. *J. Geodyn.* **94**, 20 (2020).
15. W.-J. Xu, M.-K. Zhou, M.-M. Zhao, K. Zhang, Z.-K. Hu, Quantum tiltmeter with atom interferometry. *Phys. Rev. A* **96**, 063606 (2017).
16. D. Savoie, M. Altorio, B. Fang, L. A. Sidorenkov, R. Geiger, A. Landragin, Interleaved atom interferometry for high-sensitivity inertial measurements. *Sci. Adv.* **4**, eaau7948 (2018).
17. E. R. Moan, R. A. Horne, T. Arpornthip, Z. Luo, A. J. Fallon, S. J. Berl, C. A. Sackett, Quantum rotation sensing with dual Sagnac interferometers in an atom-optical waveguide. *Phys. Rev. Lett.* **124**, 120403 (2019).
18. R. Caldwell, K. X. Weng, S. Merlet, F. Pereira Dos Santos, Simultaneous accurate determination of both gravity and its vertical gradient. *Phys. Rev. A* **99**, 033601 (2019).
19. C. Janvier, V. Ménoret, B. Desruelle, S. Merlet, A. Landragin, F. Pereira Dos Santos, Compact differential gravimeter at the quantum projection-noise limit. *Phys. Rev. A* **105**, 022801 (2022).
20. K. Bongs, M. Holyński, J. Vovrosh, P. Bouyer, G. Condon, E. Rasel, C. Schubert, W. P. Schleich, A. Roura, Taking atom interferometric quantum sensors from the laboratory to real-world applications. *Nat. Rev. Phys.* **1**, 731–739 (2019).
21. Y. Bidel, N. Zahzam, C. Blanchard, A. Bonnin, M. Cadoret, A. Bresson, D. Rouxel, M. F. Lequentrec-Lalancette, Absolute marine gravimetry with matter-wave interferometry. *Nat. Commun.* **9**, 627 (2018).
22. B. Barrett, P. Cheiney, B. Battelier, F. Napolitano, P. Bouyer, Multidimensional atom optics and interferometry. *Phys. Rev. Lett.* **122**, 043604 (2019).
23. M. Gersemann, M. Gebbe, S. Abend, C. Schubert, E. M. Rasel, Differential interferometry using a Bose-Einstein condensate. *Eur. Phys. J. D* **74**, 203 (2020).
24. B. Canuel, F. Leduc, D. Holleville, A. Gauguier, J. Fils, A. Virdis, A. Clairon, N. Dimarcq, C. J. Bordé, A. Landragin, P. Bouyer, Six-axis inertial sensor using cold-atom interferometry. *Phys. Rev. Lett.* **97**, 010402 (2006).
25. S. M. Dickerson, J. M. Hogan, A. Sugarbaker, D. M. S. Johnson, M. A. Kasevich, Multiaxis inertial sensing with long-time point source atom interferometry. *Phys. Rev. Lett.* **111**, 083001 (2013).
26. X. Wu, F. Zi, J. Dudley, R. J. Bilotta, P. Canoza, H. Müller, Multiaxis atom interferometry with a single-diode laser and a pyramidal magneto-optical trap. *Optica* **4**, 1545 (2017).
27. Y.-J. Chen, A. Hansen, G. W. Hoth, E. Ivanov, B. Pelle, J. Kitching, E. A. Donley, Single-source multiaxis cold-atom interferometer in a centimeter-scale cell. *Phys. Rev. Appl.* **12**, 014019 (2019).
28. R. Gautier, M. Guessoum, L. A. Sidorenkov, Q. Bouton, A. Landragin, R. Geiger, Accurate measurement of the Sagnac effect for matter waves. *Sci. Adv.* **8**, eabn8009 (2022).
29. S. Merlet, J. le Gouët, Q. Bodart, A. Clairon, A. Landragin, F. Pereira Dos Santos, P. Rouchon, Operating an atom interferometer beyond its linear range. *Metrologia* **46**, 87–94 (2009).
30. B. Barrett, L. Antoni-Micollier, L. Chichet, B. Battelier, T. Lévêque, A. Landragin, P. Bouyer, Dual matter-wave inertial sensors in weightlessness. *Nat. Commun.* **7**, 13786 (2016).
31. P. Cheiney, L. Fouché, S. Templier, F. Napolitano, B. Battelier, P. Bouyer, B. Barrett, Navigation-compatible hybrid quantum accelerometer using a Kalman filter. *Phys. Rev. Appl.* **10**, 034030 (2018).
32. J. Yang, W. Wu, Y. Wu, J. Lian, Improved iterative calibration for triaxial accelerometers based on the optimal observation. *Sensors* **12**, 8157–8175 (2012).
33. K. U. Schreiber, T. Klügel, G. E. Stedman, Earth tide and tilt detection by a ring laser gyroscope. *J. Geophys. Res. Solid Earth* **108**, 2132 (2003).
34. L. Timmen, H.-G. Wenzel, in *Gravity and Geoid*, H. Sünkel, I. Marson, Eds. (Springer, 1995), pp. 92–101.
35. B. Battelier, B. Barrett, L. Fouché, L. Chichet, L. Antoni-Micollier, H. Porte, F. Napolitano, J. Lautier, A. Landragin, P. Bouyer, Development of compact cold-atom sensors for inertial navigation, in *Proceedings of SPIE Quantum Optics* (SPIE, 2016), vol. 9900, p. 990004.
36. J. Lautier, L. Volodimer, T. Hardin, S. Merlet, M. Lours, F. Pereira Dos Santos, A. Landragin, Hybridizing matter-wave and classical accelerometers. *Appl. Phys. Lett.* **105**, 144102 (2014).
37. D. H. Titterton, J. L. Weston, *Strapdown Inertial Navigation Technology* (Radar, Sonar, and Navigation Series, Institution of Engineering and Technology, ed. 2, 2004).
38. T. Lévêque, A. Gauguier, F. Michaud, F. Pereira Dos Santos, A. Landragin, Enhancing the area of a Raman atom interferometer using a versatile double-diffraction technique. *Phys. Rev. Lett.* **103**, 080405 (2009).
39. S. Hartmann, J. Jenewein, E. Giese, S. Abend, A. Roura, E. M. Rasel, W. P. Schleich, Regimes of atomic diffraction: Raman versus Bragg diffraction in retroreflective geometries. *Phys. Rev. A* **101**, 053610 (2020).
40. S. Templier, J. Hauden, P. Cheiney, F. Napolitano, H. Porte, P. Bouyer, B. Barrett, B. Battelier, Carrier-suppressed multiple-single-sideband laser source for atom cooling and interferometry. *Phys. Rev. Appl.* **16**, 044018 (2021).
41. A. Peters, K. Y. Chung, S. Chu, High-precision gravity measurements using atom interferometry. *Metrologia* **38**, 25–61 (2001).
42. B. Barrett, A. Carew, S. Beattie, A. Kumarakrishnan, Measuring the atomic recoil frequency using a modified grating-echo atom interferometer. *Phys. Rev. A* **87**, 033626 (2013).
43. R. Karcher, A. Imanaliev, S. Merlet, F. Pereira Dos Santos, Improving the accuracy of atom interferometers with ultracold sources. *New J. Phys.* **20**, 113041 (2018).
44. A. Gauguier, T. E. Mehlstäubler, T. Lévêque, J. le Gouët, W. Chaibi, B. Canuel, A. Clairon, F. Pereira Dos Santos, A. Landragin, Off-resonant Raman transition impact in an atom interferometer. *Phys. Rev. A* **78**, 043615 (2008).
45. A. Louchet-Chauvet, T. Farah, Q. Bodart, A. Clairon, A. Landragin, S. Merlet, F. Pereira Dos Santos, The influence of transverse motion within an atomic gravimeter. *New J. Phys.* **13**, 065025 (2011).
46. A. Bonnin, N. Zahzam, Y. Bidel, A. Bresson, Characterization of a simultaneous dual-species atom interferometer for a quantum test of the weak equivalence principle. *Phys. Rev. A* **92**, 023626 (2015).
47. P. D. Groves, *Principles of GNSS, Inertial, and Multisensor Integrated Navigation Systems* (GNSS Technology and Applications Series, Artech House, ed. 2, 2013).
48. H. C. Lefèvre, *The Fiber-Optic Gyroscope* (Artech House, ed. 2, 2014).
49. D. Gao, B. Hu, L. Chang, F. Qin, X. Lyu, An aided navigation method based on strapdown gravity gradiometer. *Sensors* **21**, 829 (2021).
50. X. Wang, C. Gilliam, A. Kealy, J. Close, B. Moran, Probabilistic map matching for robust inertial navigation aiding. arXiv:2203.16932 [cs.RO] (31 March 2022).
51. L. Zhao, J. Li, J. Cheng, C. Jia, Q. Wang, A method for oscillation errors restriction of SINS based on forecasted time series. *Sensors* **15**, 17433–17452 (2015).
52. J. Liu, W. J. Xu, C. Zhang, Q. Luo, Z. K. Hu, M. K. Zhou, Sensitive quantum tiltmeter with nanoradian resolution. *Phys. Rev. A* **105**, 013316 (2022).
53. C. Schmelzbach, S. Donner, H. Igel, D. Sollberger, T. Taufiqurrahman, F. Bernauer, M. Häusler, C. van Renterghem, J. Wassermann, J. Robertsson, Advances in 6C seismology: Applications of combined translational and rotational motion measurements in global and exploration seismology. *Geophysics* **83**, WC53–WC69 (2018).
54. C. Van Renterghem, C. Schmelzbach, D. Sollberger, J. O. Robertsson, Spatial wavefield gradient-based seismic wavefield separation. *Geophys. J. Int.* **212**, 1588–1599 (2017).
55. M. Reinwald, M. Bernauer, H. Igel, S. Donner, Improved finite-source inversion through joint measurements of rotational and translational ground motions: A numerical study. *Solid Earth* **7**, 1467–1477 (2016).
56. Z. Li, M. van der Baan, Elastic passive source localization using rotational motion. *Geophys. J. Int.* **211**, 1206–1222 (2017).
57. S. Templier, “Three-axis hybridized quantum accelerometer for inertial navigation,” thesis, l’Université de Bordeaux (2021).
58. S. Rosi, A. Burchianti, S. Conclave, D. S. Naik, G. Roati, C. Fort, F. Minardi, Λ -enhanced grey molasses on the D2 transition of rubidium-87 atoms. *Sci. Rep.* **8**, 1301 (2018).
59. A. Keshet, W. Ketterle, A distributed, graphical user interface based, computer control system for atomic physics experiments. *Rev. Sci. Instrum.* **84**, 015105 (2013).
60. J. M. Hogan, D. M. S. Johnson, M. A. Kasevich, Atom optics and space physics, in *Proceedings of the International School of Physics “Enrico Fermi”*, E. Arimondo, W. Ertmer, W. P. Schleich, E. M. Rasel, Eds. (IOS; SIF, 2009), vol. 168, pp. 411–447.
61. R. E. Stoner, D. Butts, J. Kinast, B. Timmons, Analytical framework for dynamic light pulse atom interferometry at short interrogation times. *J. Opt. Soc. Am. B* **28**, 2418 (2011).
62. J. Saywell, I. Kuprov, D. Goodwin, M. Carey, T. Freegarde, Optimal control of mirror pulses for cold-atom interferometry. *Phys. Rev. A* **98**, 023625 (2018).
63. P. Gillot, B. Cheng, S. Merlet, F. Pereira Dos Santos, Limits to the symmetry of a Mach-Zehnder-type atom interferometer. *Phys. Rev. A* **93**, 013609 (2016).

Acknowledgments: We would like to thank O. Jolly of iXblue for assistance in developing the FPGA electronics for the RT system. The principles behind the hybrid accelerometer triad and the RT compensation system have been patented (U.S. Patent no. US11175139B2 and European Patent application no. EP18709698.7A). P.B. acknowledges support by the Dutch National Growth Fund (NGF), as part of the Quantum Delta NL program. **Funding:** This work is

supported by the French national agencies ANR (l'Agence Nationale pour la Recherche) and DGA (Délégation Générale de l'Armement) under grant no. ANR-17-ASTR-0025-01 and ESA (European Space Agency) under grant no. NAVISP-EL1-013. P.B. thanks Conseil Régional d'Aquitaine for the Excellence Chair. **Author contributions:** P.B., F.N., H.P., B.Bat., and B.Bar. conceived the project. S.T., P.C., and B.Bar. built the apparatus. S.T., P.C., Q.d.d.C., B.G., and B.Bar. performed experiments. S.T. and B.Bar. carried out the data analysis. All authors contributed to the writing of the manuscript. **Competing interests:** The authors declare that they have no competing interests. **Data and materials availability:** All data needed to

evaluate the conclusions in the paper are present in the paper and/or the Supplementary Materials. Raw data are available at the following repository: [10.5281/zenodo.7043392](https://zenodo.org/record/7043392).

Submitted 28 June 2022
Accepted 19 September 2022
Published 9 November 2022
[10.1126/sciadv.add3854](https://doi.org/10.1126/sciadv.add3854)